Real-time prediction of respiratory motion based on a local dynamic model in an augmented space

2011 Phys. Med. Biol. 56 1775

(http://iopscience.iop.org/0031-9155/56/6/016)

IOP PUBLISHING PHYSICS IN MEDICINE AND BIOLOGY

Phys. Med. Biol. **56** (2011) 1775–1789 doi:10.1088/0031-9155/56/6/016

Real-time prediction of respiratory motion based on a local dynamic model in an augmented space

S-M Hong[1], B-H Jung[2] and D Ruan[3]

[1] School of Electronics Engineering, Kyungpook National University, Deagu, Korea
[2] Department of Information and Communication, Yongin Songdam College, Yongin, Korea
[3] Department of Radiation Oncology, University of California, Los Angeles, CA, USA

E-mail: smhong@ee.knu.ac.kr, bhjung@ysc.ac.kr and druan@mednet.ucla.edu

Received 26 September 2010, in final form 30 January 2011
Published 23 February 2011
Online at stacks.iop.org/PMB/56/1775

Abstract

Motion-adaptive radiotherapy aims to deliver ablative radiation dose to the tumor target with minimal normal tissue exposure, by accounting for real-time target movement. In practice, prediction is usually necessary to compensate for system latency induced by measurement, communication and control. This work focuses on predicting respiratory motion, which is most dominant for thoracic and abdominal tumors. We develop and investigate the use of a local dynamic model in an augmented space, motivated by the observation that respiratory movement exhibits a locally circular pattern in a plane augmented with a delayed axis. By including the angular velocity as part of the system state, the proposed dynamic model effectively captures the natural evolution of respiratory motion. The first-order extended Kalman filter is used to propagate and update the state estimate. The target location is predicted by evaluating the local dynamic model equations at the required prediction length. This method is complementary to existing work in that (1) the local circular motion model characterizes 'turning', overcoming the limitation of linear motion models; (2) it uses a natural state representation including the local angular velocity and updates the state estimate systematically, offering explicit physical interpretations; (3) it relies on a parametric model and is much less data-satiate than the typical adaptive semiparametric or nonparametric method. We tested the performance of the proposed method with ten RPM traces, using the normalized root mean squared difference between the predicted value and the retrospective observation as the error metric. Its performance was compared with predictors based on the linear model, the interacting multiple linear models and the kernel density estimator for various combinations of prediction lengths and observation rates. The local dynamic model based approach provides the best performance for short to medium prediction lengths under relatively low observation rate. Sensitivity analysis indicates its robustness toward the choice of parameters. Its simplicity, robustness and low computation cost makes the

proposed local dynamic model an attractive tool for real-time prediction with system latencies below 0.4 s.

(Some figures in this article are in colour only in the electronic version)

1. Introduction

Motion management is critical in adaptive radiotherapy, where the treatment beam is controlled in response to the real-time location of the tumor target, by either gating (Keall *et al* 2002) or tracking (Nuyttens *et al* 2006). Regardless of the specific mechanism for real-time control, it is important to compensate for the corresponding system latency caused by mechanical adjustment, data communication and processing. This study focuses on investigating real-time prediction of respiratory motion—the dominant motion mode for thoracic and abdominal tumors.

The problem of predicting respiratory motion has been intensively studied. The category of parametric models often relies on local linear assumptions or its extension to autoregressive moving average (ARMA) models. Such study gives rise to direct application of the Kalman filter and multiple models (McCall *et al* 2007, McMahon *et al* 2007, Sharp *et al* 2004, Putra *et al* 2008). Effort has also been made in performing the regression in a different representation space, such as with respect to the sinusoidal (Vedam *et al* 2004) or wavelet basis (Ernst *et al* 2007). Parametric models enjoy the advantage of simplicity, low data burden and often permit efficient recursive algorithms in updating the parameters of interest. Meanwhile, nonparametric inference models relax explicit assumptions of local dynamics, and rely on consistency to 'learn' the future behavior from previous observations (Isaksson *et al* 2005, Kakar *et al* 2005, Murphy and Dieterich 2006, Ruan *et al* 2007, Ruan 2010, Ruan and Keall 2010). The nonparametric methods often require intensive training on a large dataset, and usually demand relatively heavy computation in real-time. To achieve feasibility and flexibility simultaneously, one needs to handle with care the intrinsic trade-off between the large amount of data to establish a reliable training set versus the requirement for fast response and update.

This study aims to investigate and develop an approach to perform well in the short-to-middle prediction length region, under a low data rate condition. This covers most practical situations of gating-based adaptive treatment as well as non-image based tracking, where the system latency is relatively short. The key idea here is to use a local dynamic model in an augmented space so to address 'turning' locally when indicated by the immediate preceding observations. The main novelty of this work lies in the design of the state space and the proposed local circular motion (LCM) model. The first-order extended Kalman filter (EKF) is used for the purpose of state estimation and prediction.

For simplicity and clarity, we present the proposed model in one-dimensional spatial coordinate in this paper. Extension to higher dimension can be achieved by applying the proposed method along each coordinate separately. Section 2 introduces the local characterization of the respiratory motion and the corresponding EKF scheme. Section 3 provides data details and simulation results. Finally, we conclude with a brief technical discussion.

2. Methods

In this section, we propose a local characterization of respiratory motion in an augmented space and present a prediction method based on such characterization.

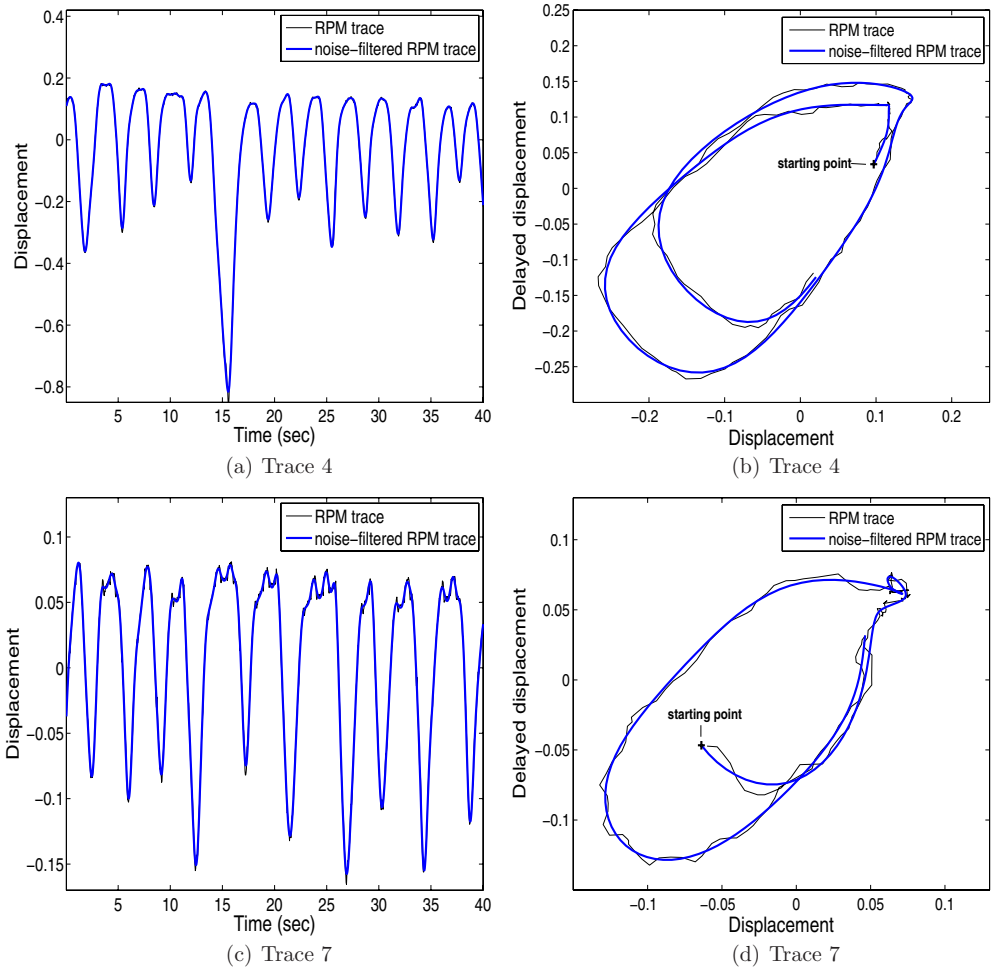

(a) Trace 4 (b) Trace 4

(c) Trace 7 (d) Trace 7

Figure 1. Left column: RPM traces, original (thin solid line) and noise-filtered (solid line); right column: 6 s segment of the trace in augmented space with 0.4 s delay, original (thin solid line) and noise-filtered (solid line).

2.1. Modeling background

Breathing motion has a semi-periodic pattern due to drifts in mean, frequency and phase. Ruan (2010) and Ruan *et al* (2007, 2008) used augmented coordinates to capture the local dynamics of breathing motion, consisting of a coordinate axis of the current observation and an augmented axis of a past observation of a fixed temporal delay. In the augmented coordinate plane, trajectories of breathing motion have been observed to have a pattern of time-varying quasi-ellipses. Figure 1 illustrates traces clinically obtained, the corresponding noise-filtered traces, and typical patterns of the clinical and noise-filtered traces in the augmented coordinate plane. The difference between RPM and noise-filtered RPM traces is marginal and barely noticeable in figures 1(a) and (c). The patterns in the augmented coordinate plane were obtained for the RPM traces over the time interval (17 s, 23 s), to illustrate the local dynamics. The clinical trace data were obtained with the real position management system (RPM system,

Varian Medical, Palo Alto, CA) at 30 Hz sampling rate. The noise-filtered traces were obtained by passing the clinical traces through a low-pass filter described in section 3. The unit of displacement is RPM-relative and dimensionless.

The quasi-elliptical pattern in the plane augmented with the delayed coordinate axis is originated from the semi-periodic evolution of respiratory motion. Motivated by this observation, we model respiratory motion as a one-dimensional projection of a curvilinear motion in a plane augmented with an independent auxiliary axis rather than the delayed axis. This alternative setup provides a much more efficient model structure, yet carries the delay-augmentation intuition. Local motion along a curvilinear trajectory can be represented in terms of a circular motion. The key idea of this work is to utilize these structural observations in solving the prediction problem. We characterize the local respiratory behavior with a circular motion model in the alternative augmented plane and incorporate the dynamical structure into a Bayesian formulation. Introducing angular velocity in the augmented dynamic space encodes the locally circular behavior into the dynamic model and captures the natural evolution of breathing motion. This characterization distinguishes the current work from previous linear models based on local linear dynamics assumptions. The latter often fail to predict 'turning' behavior of respiratory motion.

2.2. Representations of planar circular motion

A planar curve can be approximated locally by an arc of a circle, and local motion along a curve can be represented approximately in terms of a circular motion. We first consider the local motion as a uniform circular motion with constant speed and turning with constant angular rate. The assumption on the uniformity will be relaxed in the following section, and both the speed and the angular velocity will be allowed to evolve over time. Let $\Omega(t)$ denote the angular velocity. Then, the uniform circular motion in the x–y plane can be described in a differential form (Greenwood 1987):

$$\ddot{x}(t) = -\Omega(t)\,\dot{y}(t), \tag{1a}$$

$$\ddot{y}(t) = \Omega(t)\,\dot{x}(t), \tag{1b}$$

$$\dot{\Omega}(t) = 0. \tag{1c}$$

The center of the circular trajectory of the differential equations (1) remains constant, but not necessarily at the origin of the x–y plane. Equations (1) can be represented in a discrete-time form as

$$x(k+1) = x(k) + \frac{\sin\Omega(k)T}{\Omega(k)}\,\dot{x}(k) - \frac{1-\cos\Omega(k)T}{\Omega(k)}\,\dot{y}(k), \tag{2a}$$

$$\dot{x}(k+1) = \cos\Omega(k)T\,\dot{x}(k) - \sin\Omega(k)T\,\dot{y}(k), \tag{2b}$$

$$y(k+1) = y(k) + \frac{1-\cos\Omega(k)T}{\Omega(k)}\dot{x}(k) + \frac{\sin\Omega(k)T}{\Omega(k)}\,\dot{y}(k), \tag{2c}$$

$$\dot{y}(k+1) = \sin\Omega(k)T\,\dot{x}(k) + \cos\Omega(k)T\,\dot{y}(k), \tag{2d}$$

$$\Omega(k+1) = \Omega(k), \tag{2e}$$

where k denotes the discrete-time index corresponding to $t = kT$ with a uniform interval T. Derivation of (2) can be found in the appendix. The first two equations describe the evolution of position and velocity along one coordinate of the augmented space, while the next two

prescribe the dynamics for the other dimension. The position $x(k+1)$ is the physical quantity of interest, and it will be used to describe respiratory motion in the following section. It evolves based on its current value and the velocities $\dot{x}(k)$ and $\dot{y}(k)$, whose temporal behaviors are fully captured by (2*b*) and (2*d*).

Defining the discrete-time state vector by $\boldsymbol{x}(k) = [x(k)\, \dot{x}(k)\, \dot{y}(k)\, \Omega(k)]^T$,[4] we can write a discrete-time state equation to characterize the evolution of $x(k)$ as

$$\boldsymbol{x}(k+1) \;=\; \boldsymbol{f}(\boldsymbol{x}(k)), \tag{3}$$

where

$$\boldsymbol{f}(\boldsymbol{x}(k)) \;=\; \begin{bmatrix} 1 & \frac{\sin \Omega(k)T}{\Omega(k)} & -\frac{1-\cos \Omega(k)T}{\Omega(k)} & 0 \\ 0 & \cos \Omega(k)T & -\sin \Omega(k)T & 0 \\ 0 & \sin \Omega(k)T & \cos \Omega(k)T & 0 \\ 0 & 0 & 0 & 1 \end{bmatrix} \boldsymbol{x}(k). \tag{4}$$

The evolution of position $x(k)$ is the projection of the planar circular motion onto the x-coordinate. The y-axis is an auxiliary axis augmented to define the circular motion.

2.3. Modeling of respiratory motion

We use $x(k)$ to denote the unknown true position of a respiratory motion at time instant $t = kT$. The observation of $x(k)$ is modeled noise-corrupted:

$$z(k) \;=\; x(k) + w(k), \tag{5}$$

where $z(k)$ is the observation at time k and $w(k)$ denotes the corresponding additive measurement noise. The set of observations up to time k is denoted by $Z^k = \{z(1), z(2), \ldots, z(k)\}$. The goal is to predict the position at time $kT + \tau$ ($\tau > 0$), based on the measurement set Z^k.

The LCM model was introduced in (3). However, deviations are inevitable from the local motion model as the respiratory states evolve. We accommodate such deviations by introducing an additive process noise vector $\boldsymbol{v}(k)$ in (3), and allowing it to drive the evolution process via

$$\boldsymbol{x}(k+1) \;=\; \boldsymbol{f}(\boldsymbol{x}(k)) + \boldsymbol{v}(k), \tag{6}$$

with the map $f(\cdot)$ given by (4). For simplicity, we assume that the process noise vector $\boldsymbol{v}(k)$ is a zero-mean white sequence, and assume that the noise components contributing to $\dot{x}(k+1)$, $\dot{y}(k+1)$ and $\Omega(k+1)$ are mutually uncorrelated. Specifically, we assume that the covariance matrix of the noise is given by

$$\boldsymbol{Q}(k) = E[\boldsymbol{v}(k)\boldsymbol{v}^T(k)] \;=\; \begin{bmatrix} \frac{1}{3}q_1T^3 & \frac{1}{2}q_1T^2 & 0 & 0 \\ \frac{1}{2}q_1T^2 & q_1T & 0 & 0 \\ 0 & 0 & q_2T & 0 \\ 0 & 0 & 0 & q_3T \end{bmatrix}. \tag{7}$$

Here, the parameters q_i, $i = 1, 2, 3$, are the power spectral densities of the continuous counterparts of the last three components of $\boldsymbol{v}(k)$. These parameters each characterize the strength of possible changes in $\dot{x}(k)$, $\dot{y}(k)$ and $\Omega(k)$ over the sampling interval T. Since $\Omega(k)$ is the sum of a white noise sequence with variance q_3T, it becomes a discrete-time Wiener process. This process noise vector $\boldsymbol{v}(k)$ accommodates temporal changes in mean position and allows the angular velocity to evolve gradually as well.

[4] Throughout this paper, vector and matrix transposes are indicated by a superscript T.

The discrete-time observation model (5) can be formalized in terms of $\boldsymbol{x}(k)$ as

$$z(k) = \boldsymbol{H}\boldsymbol{x}(k) + w(k), \tag{8}$$

where $\boldsymbol{H} = [1\,0\,0\,0]$. The measurement noise $w(k)$ is modeled as a sequence of zero-mean white noise with variance $R(k)$. Under these assumptions, the state equation (6) and the measurement equation (8) form a stochastic discrete-time dynamic system in a standard form:

$$\begin{aligned} \boldsymbol{x}(k+1) &= \boldsymbol{f}(\boldsymbol{x}(k)) + \boldsymbol{v}(k), \\ z(k) &= \boldsymbol{H}\boldsymbol{x}(k) + w(k). \end{aligned} \tag{9}$$

We further assume the noise sequences $\boldsymbol{v}(k)$ and $w(k)$, and the initial state $\boldsymbol{x}(0)$ to be mutually independent. Note that the state equation is nonlinear. The prediction of the future position $x(kT+\tau)$, based on the measurement set Z^k, requires a nonlinear estimation. In the following section, we describe steps for the prediction using the first-order EKF.

2.4. Prediction of respiratory motion

The first-order EKF is one of the simplest structures for implementing a nonlinear estimator (Ristic *et al* 2004). It relies on a first-order expansion of the nonlinear state dynamics $\boldsymbol{f}(\boldsymbol{x}(k))$, and calculates the state estimate and its covariance matrix recursively. Let $\hat{\boldsymbol{x}}(k|k)$ denote an approximate conditional mean of the state $\boldsymbol{x}(k)$ given the observation set Z^k and let $\boldsymbol{P}(k|k)$ denote its associated covariance. One cycle of the first-order EKF, evolving $\hat{\boldsymbol{x}}(k|k)$ and $\boldsymbol{P}(k|k)$ into $\hat{\boldsymbol{x}}(k+1|k+1)$ and $\boldsymbol{P}(k+1|k+1)$, can be described as follows (Grewal and Andrews 1993, Bar-Shalom *et al* 2001).

Time update

The one-step predicted state and the corresponding covariance are given by

$$\begin{aligned} \hat{\boldsymbol{x}}(k+1|k) &= \boldsymbol{f}(\hat{\boldsymbol{x}}(k|k)), \\ \boldsymbol{P}(k+1|k) &= \boldsymbol{f}_{\boldsymbol{x}}(k)\boldsymbol{P}(k|k)\boldsymbol{f}_{\boldsymbol{x}}(k)^T + \boldsymbol{Q}(k), \end{aligned} \tag{10}$$

where $\boldsymbol{f}_{\boldsymbol{x}}(k)$ is the Jacobian of the vector $\boldsymbol{f}(\boldsymbol{x})$ evaluated at $\hat{\boldsymbol{x}}(k|k)$,

$$\boldsymbol{f}_{\boldsymbol{x}}(k) = \left[\begin{array}{cccc} 1 & \frac{\sin\Omega(k)T}{\Omega(k)} & -\frac{1-\cos\Omega(k)T}{\Omega(k)} & f_{1\Omega}(k) \\ 0 & \cos\Omega(k)T & -\sin\Omega(k)T & f_{2\Omega}(k) \\ 0 & \sin\Omega(k)T & \cos\Omega(k)T & f_{3\Omega}(k) \\ 0 & 0 & 0 & 1 \end{array}\right]\Bigg|_{\boldsymbol{x}(k)=\hat{\boldsymbol{x}}(k|k)}.$$

Here, the partial derivatives with respect to $\Omega(k)$, $f_{i\Omega}(k)$, $i = 1, 2, 3$, are given by

$$\begin{aligned} f_{1\Omega}(k) = {} & \frac{1}{\Omega(k)^2}\{(\Omega(k)T\cos\Omega(k)T - \sin\Omega(k)T)\dot{x}(k) - (\Omega(k)T\sin\Omega(k)T - \\ & 1 + \cos\Omega(k)T)\dot{y}(k)\}, \\ f_{2\Omega}(k) = {} & -T\sin\Omega(k)T\dot{x}(k) - T\cos\Omega(k)T\dot{y}(k), \\ f_{3\Omega}(k) = {} & T\cos\Omega(k)T\dot{x}(k) - T\sin\Omega(k)T\dot{y}(k). \end{aligned}$$

The one-step predicted measurement and the corresponding covariance are given by

$$\begin{aligned} \hat{z}(k+1|k) &= \boldsymbol{H}\hat{\boldsymbol{x}}(k+1|k), \\ S(k+1) &= \boldsymbol{H}\boldsymbol{P}(k+1|k)\boldsymbol{H}^T + R(k+1). \end{aligned} \tag{11}$$

State update

The state updated with new measurement $z(k+1)$ and the corresponding covariance are given by

$$\begin{aligned} \hat{\boldsymbol{x}}(k+1|k+1) &= \hat{\boldsymbol{x}}(k+1|k) + \boldsymbol{K}(k+1)(z(k+1) - \hat{z}(k+1|k)), \\ \boldsymbol{P}(k+1|k+1) &= \boldsymbol{P}(k+1|k) - \boldsymbol{K}(k+1)S(k+1)\boldsymbol{K}(k+1)^T, \end{aligned} \tag{12}$$

where $\boldsymbol{K}(k+1)$ is the Kalman gain

Table 1. RPM dataset information.

Subject ID (i)	1	2	3	4	5	6	7	8	9	10
STD_i	0.49	0.50	0.30	0.20	0.32	0.17	0.07	0.23	0.28	0.11
P-P_i	2.54	2.36	1.27	1.12	1.87	0.97	0.29	0.88	1.22	0.43
$\text{P-P}_i/\text{STD}_i$	5.11	4.74	4.21	5.66	5.92	5.61	4.59	3.88	4.44	4.05
Duration (s)	140	79	113	165	165	117	150	165	160	162

$$\boldsymbol{K}(k+1) = \boldsymbol{P}(k+1|k)\boldsymbol{H}^T S(k+1)^{-1}.$$

Given $\hat{\boldsymbol{x}}(k|k)$, the position at time $kT+\tau$ ($\tau > 0$) can be predicted at the first step of the above cycle. Let $\hat{x}(kT+\tau|k)$ denote the prediction of the true position at time $kT+\tau$ based on the measurement set Z^k. The prediction is a function of τ and $\hat{\boldsymbol{x}}(k|k)$, and it can be obtained by evaluating the first component of $\hat{\boldsymbol{x}}(kT+\tau|k)$ of (10) with T in (4) replaced by τ. That is,

$$\hat{x}(kT+\tau|k) = \hat{x}(k|k) + \frac{\sin\hat{\Omega}(k|k)\tau}{\hat{\Omega}(k|k)}\hat{\dot{x}}(k|k) - \frac{1-\cos\hat{\Omega}(k|k)\tau}{\hat{\Omega}(k|k)}\hat{\dot{y}}(k|k). \quad (13)$$

Finally, it is remarked that the discrete-time system (9) does not satisfy the nonlinear observability rank condition at $\Omega(k) = 0$, which is one of the conditions to assure the boundedness of the estimation error (Reif *et al* 1999). The angular rate, however, remains away from zero at most sample points along a respiratory trajectory, and the rank condition appears not a problem in practice. This was confirmed in experiments based on clinical RPM data in section 3.

3. Experimental results and analysis

3.1. Data description

We used the RPM system to obtain one-dimensional traces of fiducial markers placed on the patient's chest wall. The RPM traces are believed to be highly correlated with respiratory motion and sufficiently capture the temporal behavior of respiration. Moreover, the performance of respiratory prediction algorithms depends on the fundamental variation pattern rather than the amplitude, so the RPM traces are reasonable test subjects for algorithmic development. To rid the adverse impact of the arbitrary scaling in RPM amplitude, we adopt the normalized root mean squared error (nRMSE) as the performance measure for each trace i, defined by the usual RMSE divided by the standard deviation (STD) of the observed sample values:

$$\text{nRMSE}_i = \frac{\text{RMSE}_i}{\text{STD}_i} = \frac{\sqrt{\frac{1}{|\mathcal{N}_i|}\sum_{k\in\mathcal{N}_i}(z_i(kT+\tau) - \hat{x}_i(kT+\tau|k))^2}}{\sqrt{\frac{1}{N_i}\sum_{k=1}^{N_i}(z_i(k) - \frac{1}{N_i}\sum_{k=1}^{N_i} z_i(k))^2}}, \quad (14)$$

where $\mathcal{N}_i$ denotes the time index set upon which the prediction was performed for trace i, and $|\mathcal{N}_i|$ denotes its cardinality. N_i denotes the number of sample points of trace i. Population nRMSE (across traces) is computed by taking the average of the trace-wise nRMSE, i.e.

$$\text{nRMSE} = \sqrt{\frac{1}{\text{number of traces}}\sum_i \text{nRMSE}_i^2}. \quad (15)$$

We report the RPM data characteristics in table 1, where STD_i and P-P_i denote the STD and the peak-to-peak displacement of trace i, respectively.

3.2. Experimental details

We implemented our predictor using the EKF based on the local motion model described in section 2. The predictor is referred to as the LCM model hereafter. The design parameters q_1, q_2 and q_3 in (7) were set to 0.2, 2×10^{-4} and 2×10^{-3}, respectively. The parameter values were chosen to minimize nRMSE of (15) for a trace separate from the testing population for 10 Hz sampling rate and 0.4 s prediction length on a coarse grid, and they were used for all combinations of the sampling rate and prediction length in our experiments. The nRMSE_i (14) was obtained for each trace after an initial warm-up phase of five samples of the EKF. Note that the number of samples for warm-up is very small and on-line 'training' is not required for the EKF.

A Chebyshev type II filter was implemented to filter out the measurement noise from the position observation of RPM traces, in order to determine the STD of the measurement noise in (9). The order of the filter was 5 and the cutoff frequency was set to 1.5 Hz. The frequency characteristic of the low-pass filter is relatively light in terms of noise filtering. The filter was used to obtain the noise-filtered RPM trace data presented in figure 1. Based on numerical experiments similar to the method described in Putra *et al* (2008), we obtained the STD of the measurement noise and set it to 10^{-2}. The characterization of the measurement noise statistics is subjective, since we cannot determine the true position from real trace data and the probabilistic distribution of the noise depends on the frequency characteristics of a low-pass filter employed. As a consequence, it is more reasonable to quantify prediction performance in terms of measurement prediction error $z_i(kT+\tau) - \hat{x}_i(kT+\tau|k)$ in (14) rather than position error against unknown true position.

We implemented for comparison an adaptive linear filter (denoted linear) (Haykin 2002) and a kernel density estimator (KDE) (Ruan 2010). The adaptive linear model is the most widely applied predictor due to its simplicity and efficiency. The KDE predictor, on the other hand, is representative of machine learning based approaches, and enjoys the advantage of flexibility and good performance for long prediction lengths. We also implemented a predictor based on the interacting multiple model (IMM) estimator following the design presented in Putra *et al* (2008). This predictor (denoted MLM) employs two Kalman filters, each matched to one of the two linear models: a constant velocity model and a constant acceleration model. The parameters of MLM were set as $Q_1 = 10$, $Q_2 = 0.5$, and $R_1 = R_2 = 10^{-4}$. The elements of the Markovian transition matrix were set to the values given in Putra *et al* (2008). The process noise variances Q_1 and Q_2 were chosen so that nRMSE of (15) could have a value near its minimum over a set of sampling rates and prediction lengths. The IMM estimator adaptively adjusts its model probabilities so that the estimator can be matched to changes of system dynamics.

3.3. Experiment results and observations

Figure 2 presents traces 4 and 7 and the corresponding trajectories predicted with MLM and the proposed LCM predictor. The figure indicates that LCM can reduce 'overshoots' and 'undershoots' in prediction more effectively than MLM. This result demonstrates the effectiveness of a circular motion model over a linear model in characterizing the local respiratory motion. Recall that MLM is implemented using the IMM estimator with two Kalman filters, each matched to a linear model. In figure 2, slight lags in the prediction are observed for both of the predictors. In general, such lags can be reduced by selecting increased process noise, but at the cost of a significant increase in overshoots and undershoots that leads to large deviations in prediction. The figure also indicates that a small number

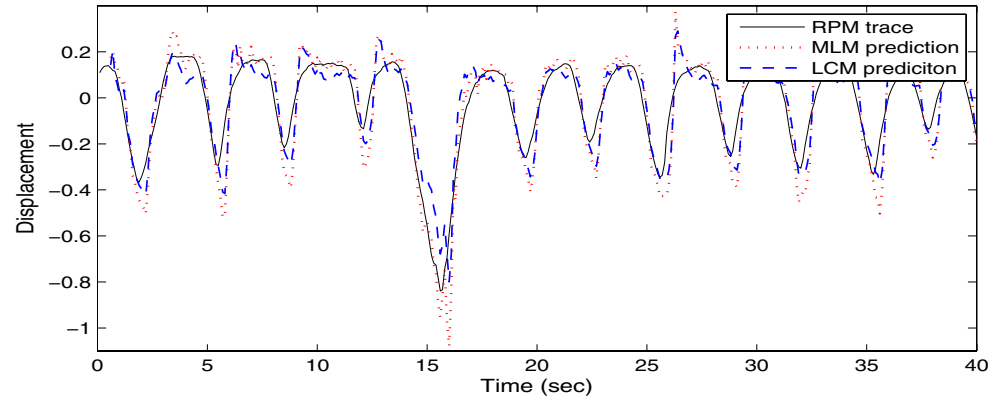

(a) Trace 4

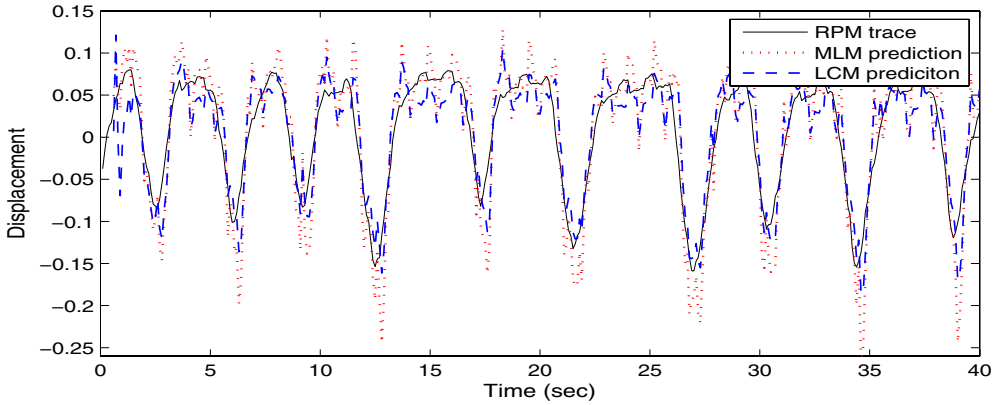

(b) Trace 7

Figure 2. Trace prediction with MLM and LCM predictors (0.4 s prediction length and 10 Hz sampling rate).

(five) of samples suffice to warm-up MLM and LCM. Figure 3 presents the same two traces and the corresponding trajectories predicted with KDE and LCM. KDE normally requires at least one-cycle worth of data for training to ensure sufficient recognition power for various breathing phases. In the figure, the KDE starts to predict the trace at 11.3 s after an initial training stage. The figure shows that the KDE predicts the respiratory motion accurately at most sample points. However, large deviations are also observed when respiratory motion changes irregularly and its behavior differs significantly from preceding one in a training window. Figure 4 reports the prediction performance in terms of normalized root mean squared difference (14) for various combinations of the prediction length and observation sampling rate. Traces 4 and 7 are the most challenging to predict, yielding the highest nRMSE throughout all prediction lengths and sampling rates in figure 4. This phenomenon can be explained by their irregular variations in mean position and frequency. Figure 5 shows the change of performance as the prediction length varies for these two traces. Figure 6 illustrates the collective performance across all traces.

It can be observed from figure 4 that the proposed LCM predictor performs uniformly better than MLM for all traces and for all the combinations of the prediction length and sampling rate in the figures. This advantage is statistically significant. We confirmed the

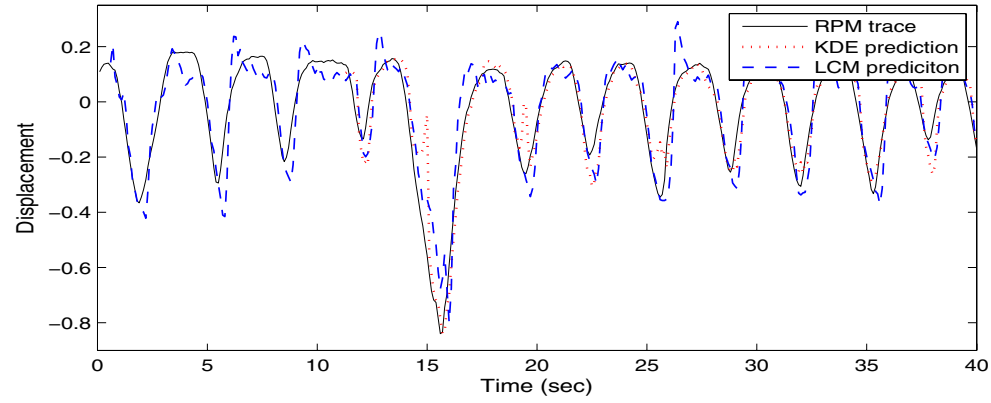

(a) Trace 4

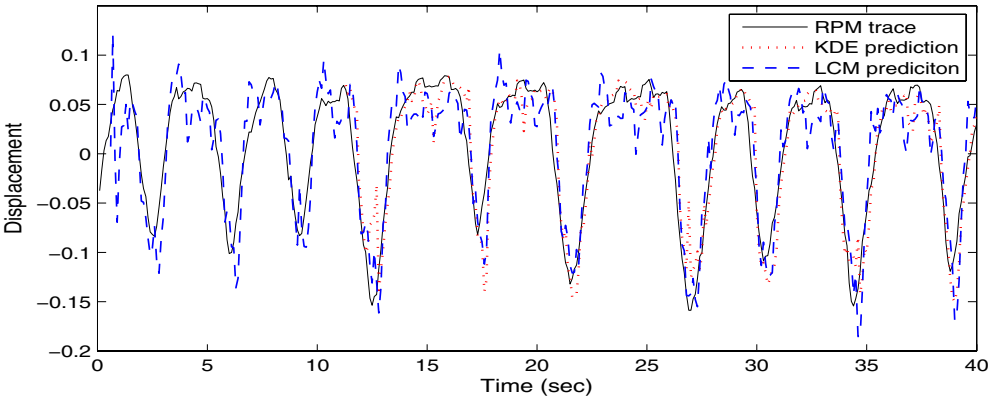

(b) Trace 7

Figure 3. Trace prediction with KDE and LCM predictors (0.4 s prediction length and 10 Hz sampling rate).

significance via the paired Student t-test that yields p-values less than 5.6×10^{-3} for all the combinations of the prediction length and sampling rate. The advantage of LCM over linear is also obvious from figure 4. The next comparison is between LCM and KDE. It can be observed from figures 4(a) and (b) that the LCM predictor outperforms the KDE predictor for a low prediction length (0.2 s) and low sampling rates (5 and 10 Hz). The paired t-test between LCM and KDE yields $p = 3.3 \times 10^{-5}$ for 5 Hz and $p = 9.2 \times 10^{-4}$ for 10 Hz. This advantage becomes less significant and finally vanishes as we move to the region of longer prediction length (the right-hand side column in figure 4) and higher observation rates (bottom rows in figure 4). The advantage of the KDE becomes more significant as the prediction length increases over 0.4 s. This observation is corroborated with figure 5, where the LCM performs the best when the prediction length is short and then becomes dominated by the KDE predictor as the prediction length increases. The comparison among various methods is summarized in table 2.

Interestingly, we can 'partition' the region of operation defined by the prediction length and sampling rate according to the best predictor with respect to nRMSE_i of (14) for each trace. More specifically, it can be observed from figure 4 that the LCM predictor offers the

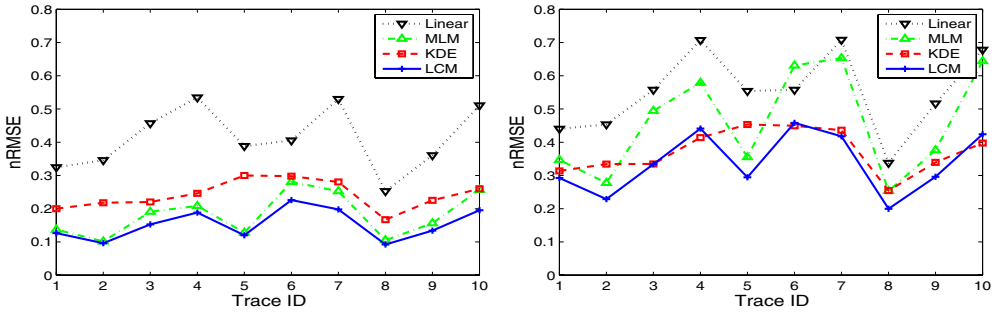

(a) Prediction length 0.2 sec (b) Prediction length 0.4 sec

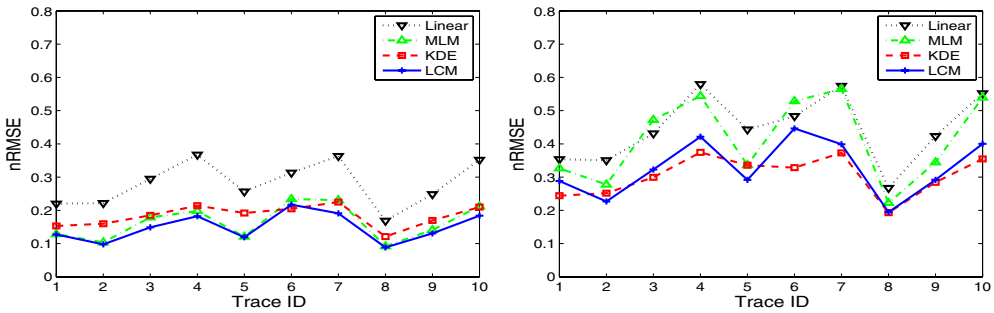

(c) Prediction length 0.2 sec (d) Prediction length 0.4 sec

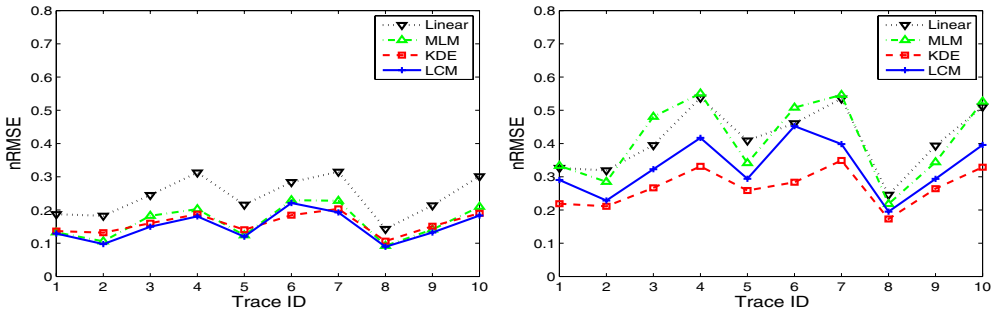

(e) Prediction length 0.2 sec (f) Prediction length 0.4 sec

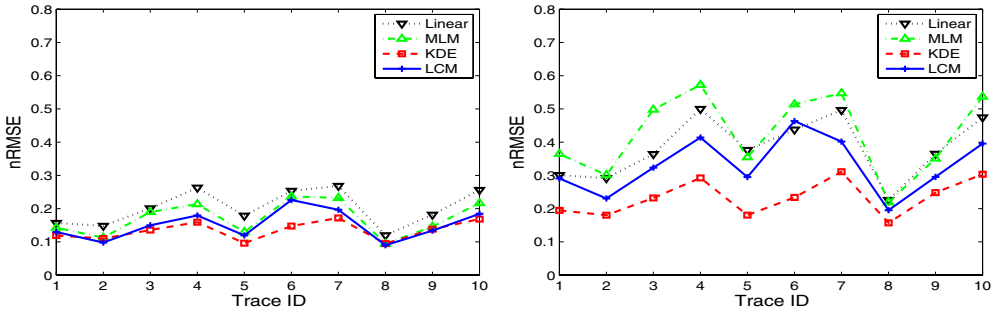

(g) Prediction length 0.2 sec (h) Prediction length 0.4 sec

Figure 4. Comparison of prediction performance in terms of nRMSE. (a), (b) At 5 Hz sampling rate; (c), (d) at 10 Hz sampling rate; (e), (f) at 15 Hz sampling rate; (g), (h) at 30 Hz sampling rate.

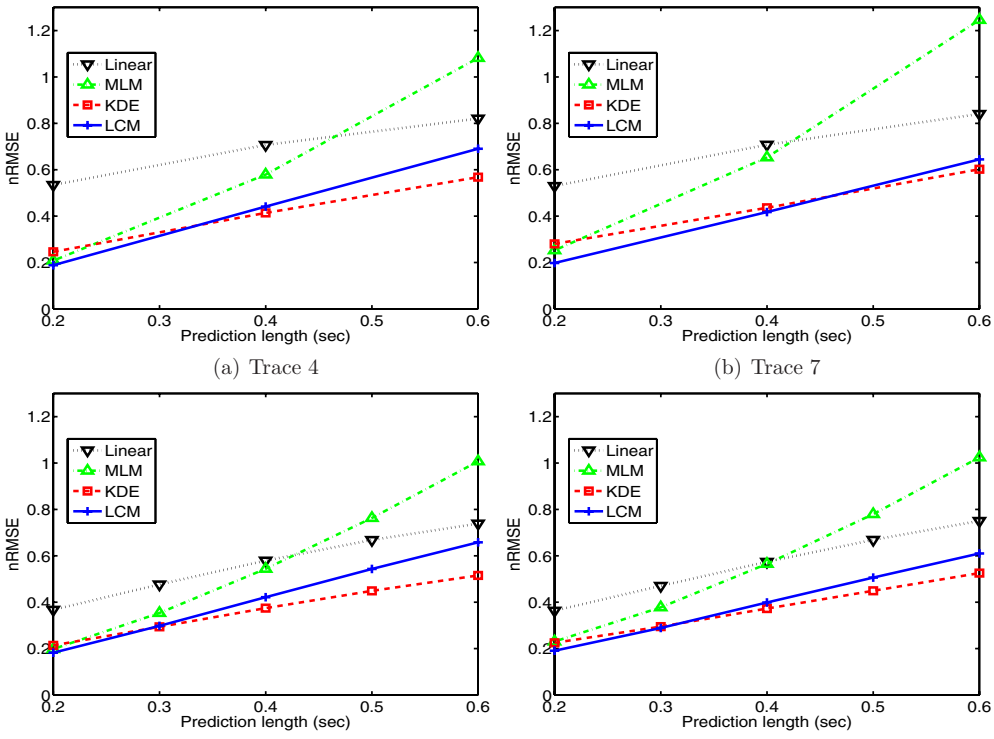

(a) Trace 4 (b) Trace 7

(c) Trace 4 (d) Trace 7

Figure 5. Performance as a function of prediction length. Upper row: 5 Hz sampling rate; bottom row: 10 Hz sampling rate.

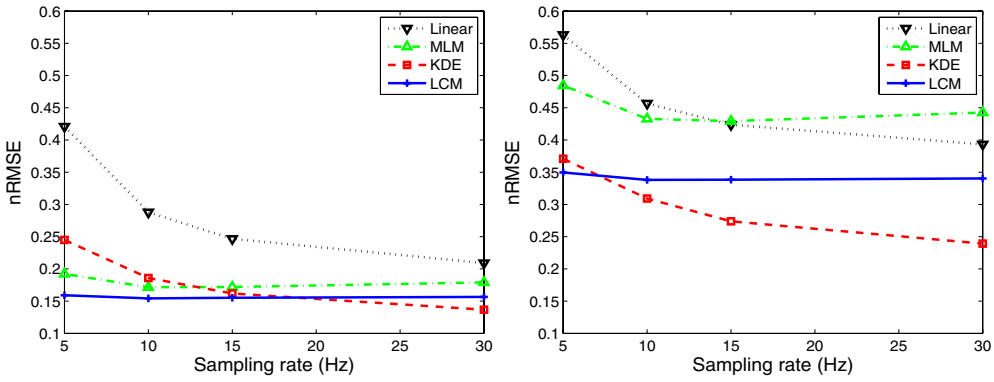

(a) Prediction length 0.2 sec (b) Prediction length 0.4 sec

Figure 6. nRMSE versus sampling rate for prediction lengths 0.2 s and 0.4 s across all traces.

best performance when the values of the prediction length and sampling rate are both low, and the KDE provides the best performance when both of these parameters are high. This implies that we can realize uniformly best prediction performance for each patient by choosing either

Table 2. Comparison among various methods.

Predictor	Training	Warm-up	Computation	Major strength	Major weakness
Linear	No	Yes	Low	Simplicity	Operate on a single linear mode
MLM	No	Yes	Low	Adaptive switching among multiple models	Inferior for long prediction during which model in action switches
KDE	Yes	No	O (# of template seeds)	Flexibility, almost constant w.r.t prediction length	Computation, single point prediction
LCM	No	Yes	Low	Consistent performance w.r.t. sampling rate	Intrinsically local, degraded performance for long prediction

the LCM or the KDE predictor. The two predictors can be concurrently executed to evaluate and compare the error (14) for a trace segment before or during radiation delivery.

The near-constant performance of the proposed LCM model with respect to the sampling rate is observed from figure 6, which is desirable for image-guided treatment. From a practical point of view, on-board imagers or portal imagers have nominal operating frame rates of 5–10 Hz to achieve reasonable image quality. Furthermore, imaging dose is roughly proportional to the total number of images taken during the whole treatment session, thus depends on the imaging rate linearly. The consistent performance of LCM with respect to the sampling rate promises imaging dose reduction without compromising prediction performance. An imaging frequency of 5–10 Hz has been suggested for imaging dose considerations (Jiang 2006). When observations are acquired at 5 Hz, the 0.2 s prediction capability of the LCM suffices to extrapolate the dynamics until the arrival of the next observation image, for monitoring the target location in real-time.

As in any estimation problems involving configuration parameters, performance robustness with respect to such parameter setting is highly desirable. In our case, the setting parameters are (q_1, q_2, q_3) and the population nRMSE (15) is not sensitive to their values. It turns out that the nRMSE values change less than 5×10^{-3} against our design for the choice of (q_1, q_2, q_3) over the set ([0.15, 2.0], $[10^{-5}, 10^{-3}]$, $[10^{-4}, 5 \times 10^{-3}]$). This statement holds for all the combinations of the prediction length and sampling rate in figure 4.

4. Conclusion and future work

This study proposes a simple predictor based on a local dynamic model. In particular, the model introduces the angular velocity into the state estimate to encode the semi-periodic evolution of respiratory motion. This novel model structure circumvents the limitation of linear models and allows the state estimates to adjust for the turning behavior in a natural fashion. The predictor performs effectively to compensate for system latency under most practical situations of gating-based adaptive treatment as well as non-image based tracking. The proposed LCM model enjoys the simplicity and is economic in terms of data requirement, offering a performance almost independent of the observation sampling rate. This desirable property complements the performance of nonparametric models such as KDE-based approaches, which require abundant data for efficient learning. As extension of this study, we will investigate the use of local dynamic models in predicting multi-dimensional signals from a holistic perspective,

rather than simplistically applying the local dynamic model to each coordinate separately. We will also explore the potential benefit of incorporating the proposed local dynamic model into a multiple model setting to further improve the prediction performance.

Acknowledgments

The authors are grateful to the reviewers for their helpful comments and suggestions. SMH was supported by BK21 program. DR was supported partially by AAPM research seed grant and AACR career development award. She thanks Dr Paul Keall for his continuous guidance and support.

Appendix: Derivation of equation (2)

Using the state vector $\boldsymbol{x}_c(t) = [x(t)\,\dot{x}(t)\,y(t)\,\dot{y}(t)\,\Omega(t)]^T$, we can rewrite equation (1) in the form of a continuous-time state equation:

$$\dot{\boldsymbol{x}}_c(t) = \begin{bmatrix} 0 & 1 & 0 & 0 & 0 \\ 0 & 0 & 0 & -\Omega(t) & 0 \\ 0 & 0 & 0 & 1 & 0 \\ 0 & \Omega(t) & 0 & 0 & 0 \\ 0 & 0 & 0 & 0 & 0 \end{bmatrix} \boldsymbol{x}_c(t). \tag{A.1}$$

Since $\Omega(t)$ is constant, we can set it to a constant Ω_0. Denoting by $\boldsymbol{A}$ the matrix of (A.1) with Ω_0, we can represent (A.1) by $\dot{\boldsymbol{x}}_c(t) = \boldsymbol{A}\,\boldsymbol{x}_c(t)$, which is a linear time-invariant system. The linear time-invariant system can be transformed into a discrete-time form as (Rugh 1996)

$$\boldsymbol{x}_c(k+1) = \exp(\boldsymbol{A}T)\,\boldsymbol{x}_c(k). \tag{A.2}$$

We use the relationship $\exp(\boldsymbol{A}T) = \mathcal{L}^{-1}[(s\boldsymbol{I} - \boldsymbol{A})^{-1}]$ to obtain the state transition matrix $\exp(\boldsymbol{A}T)$, where $\mathcal{L}^{-1}$ denotes the inverse Laplace transform and $\boldsymbol{I}$ is the identity matrix. We have

$$(s\boldsymbol{I} - \boldsymbol{A})^{-1} = \begin{bmatrix} \frac{1}{s} & \frac{1}{s^2+\Omega_0^2} & 0 & -\frac{\Omega_0}{s(s^2+\Omega_0^2)} & 0 \\ 0 & \frac{s}{s^2+\Omega_0^2} & 0 & -\frac{\Omega_0}{s^2+\Omega_0^2} & 0 \\ 0 & \frac{\Omega_0}{s(s^2+\Omega_0^2)} & \frac{1}{s} & \frac{1}{s^2+\Omega_0^2} & 0 \\ 0 & \frac{\Omega_0}{s^2+\Omega_0^2} & 0 & \frac{s}{s^2+\Omega_0^2} & 0 \\ 0 & 0 & 0 & 0 & \frac{1}{s} \end{bmatrix}, \tag{A.3}$$

and its inverse Laplace transform

$$\mathcal{L}^{-1}[(s\boldsymbol{I} - \boldsymbol{A})^{-1}] == \begin{bmatrix} 1 & \frac{\sin\Omega_0 T}{\Omega_0} & 0 & -\frac{1-\cos\Omega_0 T}{\Omega_0} & 0 \\ 0 & \cos\Omega_0 T & 0 & -\sin\Omega_0 T & 0 \\ 0 & \frac{1-\cos\Omega_0 T}{\Omega_0} & 1 & \frac{\sin\Omega_0 T}{\Omega_0} & 0 \\ 0 & \sin\Omega_0 T & 0 & \cos\Omega_0 T & 0 \\ 0 & 0 & 0 & 0 & 1 \end{bmatrix}. \tag{A.4}$$

Substituting result (A.4) into (A.2) and replacing Ω_0 by $\Omega(k)$ yields the discrete-time state equation (2). The same result can be obtained by discretizing the nonlinear system (A.1) directly (Kazantzis and Kravaris 1999).

References

Bar-Shalom Y, Li X-R and Kirubarajan T 2001 *Estimation with Applications to Tracking and Navigation* (New York: Wiley)

Ernst F, Schlaefer A and Schweikard A 2007 Prediction of respiratory motion with wavelet-based multiscale autoregression *MICCAI 2007, Part II (Lecture Notes in Computer Science* vol 4792*)* ed N Ayache, S Ourselin and A Maeder (Heidelberg: Springer) pp 668–75

Greenwood D T 1987 *Principles of Dynamics* (Englewood Cliffs, NJ: Prentice-Hall)

Grewal M S and Andrews A P 1993 *Kalman Filtering: Theory and Practice* (Englewood Cliffs, NJ: Prentice-Hall)

Haykin S 2002 *Adaptive Filter Theory* (Upper Saddle River, NJ: Prentice-Hall)

Isaksson M, Jalden J and Murphy M J 2005 On using an adaptive neural network to predict lung tumor motion during respiration for radiotherapy applications *Med. Phys.* **32** 3801–9

Jiang S 2006 Technical aspects of image-guided respiration-gated radiation therapy *Med. Dosim.* **31** 141–51

Kakar M, Nyström H, Aarup L R, Nøttrup T J and Olsen D R 2005 Respiratory motion prediction by using the adaptive neuro-fuzzy inference system (ANFIS) *Phys. Med. Biol.* **50** 4721–8

Kazantzis N and Kravaris C 1999 Time-discretization of nonlinear control systems via Taylor methods *Computers and Chem. Eng.* **23** 763–84

Keall P J, Kini V R, Vedam S S and Mohan R 2002 Potential radiotherapy improvements with respiratory gating *Australas. Phys. Eng. Sci. Med.* **25** 1–6

McCall K C and Jeraj R 2007 Dual-component model of respiratory motion based on the periodic autoregressive moving average (periodic ARMA) method *Phys. Med. Biol.* **52** 3455–66

McMahon R, Papiez L and Sandison G 2007 Addressing relative motion of tumors and normal tissue during dynamic MLC tracking delivery *Australas. Phys. Eng. Sci. Med.* **30** 331–6

Murphy M J and Dieterich S 2006 Comparative performance of linear and nonlinear neural networks to predict irregular breathing *Phys. Med. Biol.* **51** 5903–14

Nuyttens J J, Prevost J B, Praag J, Hoogeman M, Van Klaveren R J, Levendag P C and Pattynama P M 2006 Lung tumor tracking during stereotactic radiotherapy treatment with the cyberknife: marker placement and early results *Acta Oncol.* **45** 961–5

Putra D, Haas O C, Mills J A and Burnham K J 2008 A multiple model approach to respiratory motion prediction for real-time IGRT *Phys. Med. Biol.* **53** 1651–63

Reif K, Günther S, Yaz E and Unbehauen R 1999 Stochastic stability of the discrete-time extended Kalman filter *IEEE Trans. Automatic Control* **44** 714–28

Ristic B, Arulampalam S and Gordon N 2004 *Beyond the Kalman Filter: Particle Filters for Tracking Applications* (Boston, MA: Artech House Publishers)

Ruan D 2010 Kernel density estimation-based real-time prediction for respiratory motion *Phys. Med. Biol.* **55** 1311–26

Ruan D, Fessler J A and Balter J M 2007 Real-time prediction of respiratory motion based on local regression methods *Phys. Med. Biol.* **52** 7137–52

Ruan D, Fessler J A, Balter J M, Berbeco R I, Nishioka S and Shirato H 2008 Inference of hysteretic respiratory tumour motion from external surrogates: a state augmentation approach *Phys. Med. Biol.* **53** 2923–36

Ruan D and Keall P J 2010 Online prediction of respiratory motion: multidimensional processing with low-dimensional feature learning *Phys. Med. Biol.* **55** 3011–25

Rugh W J 1996 *Linear System Theory* (Upper Saddle River, NJ: Prentice-Hall) p 74

Sharp G C, Jiang S B, Shimizu S and Shirato H 2004 Prediction of respiratory tumour motion for real-time image-guided radiotherapy *Phys. Med. Biol.* **49** 425–40

Vedam S S, Keall P J, Docef A, Todor D A, Kini V R and Mohan R 2004 Predicting respiratory motion for four-dimensional radiotherapy *Med. Phys.* **31** 2274–83